Monthly Notices of the ROYAL ASTRONOMICAL SOCIETY

MNRAS **450,** 3458–3471 (2015) doi:10.1093/mnras/stv826

The infrared and molecular environment surrounding the Wolf-Rayet star WR 130

S. Cichowolski,[1★†] L. A. Suad,[2‡] S. Pineault,[3,4] A. Noriega-Crespo,[5] E. M. Arnal[2,6,★] and N. Flagey[7]

[1]*Instituto de Astronomía y Física del Espacio (IAFE), CC 67, Suc. 28, 1428 Buenos Aires, Argentina*
[2]*Instituto Argentino de Radioastronomía (CCT-La Plata, CONICET), CC 5, 1894 Villa Elisa, Argentina*
[3]*Département de physique, de génie physique et d'optique, Université Laval, Québec G1V 0A6, Canada*
[4]*Centre de Recherche en Astrophysique du Québec (CRAQ), Montréal, QC H3C 3J7, Canada*
[5]*Space Telescope Science Institute, 3700 San Martin Drive, Baltimore, MD 21218, USA.*
[6]*Facultad de Ciencias Astronómicas y Geofísicas, Universidad Nacional de La Plata, Paseo del Bosque s/n, 1900 La Plata, Argentina*
[7]*Canada–France–Hawaii Telescope Corporation, 65-1238 Mamalahoa Hwy, Kamuela, HI 96743, USA*

Accepted 2015 April 9. Received 2015 April 1; in original form 2015 January 7

ABSTRACT

We present a study of the molecular CO gas and mid/far-infrared radiation arising from the environment surrounding the Wolf–Rayet (WR) star 130. We use the multiwavelength data to analyse the properties of the dense gas and dust, and its possible spatial correlation with that of young stellar objects (YSOs). We use ^{12}CO J=1–0 data from the Five College Radio Astronomy Observatory survey as tracer of the molecular gas, and mid/far-infrared data from the recent *Wide-Field Infrared Survey Explorer* (WISE) and *Herschel* space surveys to study the dust continuum radiation and to identify a population of associated candidate YSOs. The spatial distribution of the molecular gas shows a ring-like structure very similar to that observed in the H I gas, and over the same velocity interval. The relative spatial distribution of the H I and CO components is consistent with a photodissociation region. We have identified and characterized four main and distinct molecular clouds that create this structure. Cold dust is coincident with the dense gas shown in the CO measurements. We have found several young stellar object candidates that lie along the regions with the highest gas column density, and suggest that they are spatially correlated with the shell. These are indicative of regions of star formation induced by the strong wind and ionization of the WR star.

Key words: stars: formation – stars: individual: WR 130 – ISM: bubbles – H II regions – infrared: ISM.

1 INTRODUCTION

Massive O-type stars and their descendants have a major impact on their surrounding interstellar medium (ISM) via their high throughput of ionizing photons, their energetic winds, their expanding H II regions, and their final explosion as supernova.

During their evolutionary courses, massive stars possess quite different mass-loss rates and wind speeds, generating a variety of structures such as bubbles, shells (or multishells) in the ISM (Castor, McCray & Weaver 1975; Weaver et al. 1977; Garcia-Segura & Mac Low 1995). Due to the high number of ultraviolet photons emitted by the star during the O-type phase, an H II region is formed around the star (Weaver et al. 1977). As this hot region expands, neutral material accumulates between the ionization front and the shock front that precedes it in the neutral gas (see Dyson & Williams 1997). Simultaneously with the ionization of its surroundings, stellar winds are blown by massive stars, which may affect the evolution of the H II region.

The following phase in the evolution of the star depends on its initial mass (e.g. Crowther 2007). For masses higher than ∼60 $M_\odot$ the star could go directly to a Wolf–Rayet (WR) phase, without going first through a RSG or LBV phase (e.g. Smith & Conti 2008).

During the WR phase, the stellar wind strengthens (could be an order of magnitude higher than in the main-sequence phase) and may clear the region around the ionizing star, creating a stellar-wind bubble filled with high temperature ($T \sim 10^{6-7}$ K) and low density (n $\sim 10^{-2}$–10^{-3} cm^{-3}) shocked gas. In due time, this hot cavity may drive expanding gas shells that may eventually interact with the shell related to the expanding H II region. In this way, the supersonic winds can entrain and accelerate the surrounding gas, thereby injecting momentum and energy

★Member of the Carrera del Investigador Científico of CONICET, Argentina.
†E-mail: scicho@iafe.uba.ar
‡Post-Doc Fellow of CONICET, Argentina.

© 2015 The Authors
Published by Oxford University Press on behalf of the Royal Astronomical Society

Downloaded from https://academic.oup.com/mnras/article-abstract/450/4/3458/992360 by guest on 04 September 2019

into the surrounding gaseous environment, strongly affecting its evolution.

The structures created by the action of massive stars, usually striking at radio frequencies, are also very bright at far-infrared wavelengths, due to the presence of dust grains that absorb the UV stellar photons and cool down emitting in the infrared. The so-called infrared dust bubbles can now been studied in detail since the release of the *WISE* (Wright et al. 2010), *Spitzer* (Benjamin et al. 2003; Carey et al. 2009), and *Herschel* (Molinari et al. 2010) data (e.g. Zavagno et al. 2010; Paladini et al. 2012).

One important consequence of the interaction between massive stars and their local ISM is that the physical conditions present in the dense expanding shells are ideal for star formation activity. Several studies in fact show the presence of young stellar object candidates (cYSOs) whose birth was probably triggered by the expansion of H II regions (Zavagno et al. 2010, and references there in). However, similar studies towards WR stars, representative of more evolved stages of massive stars, are scanty (Cappa et al. 2010; Liu et al. 2012; Liu, Wu & Zhang 2013). Thus, it is still unclear whether these older bubbles can create regions of active star formation around them.

In this work, we present the second part of a multiwavelength study of the surroundings of WR 130, a WN8(h) star (van der Hucht 2001) or, as proposed by Smith & Conti (2008), a WNH. The place that this type of WR stars, which are the least chemically evolved (Conti, Leep & Perry 1983), has in the evolution sequence of a massive star is not completely understood. Based on the mass discrepancy observed between WNH and H-poor WR stars (the WNH stars have higher masses), and on the fact that the most luminous WNH stars tend to be more H-rich than LBVs, Smith & Conti (2008) concluded that the WNH stars are pre-LBVs, and that via the violent eruptions of the LBV phase the star removes the hydrogen envelope and becomes a WN star. In this scenario, WR 130 could be in a pre-LBV phase. The observed impact that WR 130 has on its environment seems to support this possibility. Indeed, a very well defined ring-like H II region, first noticed by Heckathorn, Bruhweiler & Gull (1982), is associated with this star. Later, Cichowolski et al. (2001) studied the region using a multiwavelength approach that involved Dominion Radio Astrophysical Observatory (DRAO) H I line data and continuum at 408 and 1420 MHz, H110 α Very Large Array (VLA) data, HIRES 60 and 100 μm data (Fowler & Aumann 1994), and 12 and 25 μm Mid-Infrared Galaxy Atlas images (Kerton & Martin 2000). From all the data analysed, Cichowolski et al. (2001) observed a well-defined ring-like structure, which is consistent with a scenario were the action of the O star was directly followed by the action of the WR star, since the material expected to be present if the LBV phase took place is not detected. In this paper, we now present a study of the CO clouds detected in the area of WR 130 and analyse the properties of the dust making use of the new available *WISE* and *Herschel* data, which allow us to provide new insights into the gas and dust properties of the ISM surrounding a WR star. We also search for the presence of triggered star formation towards the surroundings of WR 130.

2 OBSERVATIONS

In this paper, we use the 1420 MHz radio continuum image of the WR 130 area from the Canadian Galactic Plane Survey (CGPS – Taylor et al. 2003). Because this image is the result of a mosaic containing more than one pointing field, it has a slightly better signal-to-noise ratio and dynamic range. It also has better flux and position registration, and a slightly better resolution, factors which are important when estimating the fluxes of some discrete sources seen projected over an inhomogeneous background.

At infrared wavelengths, we have used the data retrieved from the *Wide-Field Infrared Survey Explorer* (WISE; Wright et al. 2010), which is an all-sky survey that contains images in four infrared channels centred at 3.4, 4.6, 12, and 22 μm. These channels, respectively, have angular resolutions of 6.1, 6.4, 6.5, and 12 arcsec. We obtained all the images from the NASA/IPAC Infrared Science Archive (http://irsa.ipac.caltech.edu).

We have also included *Herschel* data (Pilbratt et al. 2010) from the *Herschel* Infrared Galactic Plane Survey (HiGAL; Molinari et al. 2010) obtained in its five photometric bands at 70 and 160 μm with PACS (Poglitsch et al. 2010), plus 250, 350, and 500 μm with SPIRE (Griffin et al. 2010). The maps have been produced by the improved version of the ROMAGAL pipeline using UNIMAP, and therefore, are optimized to preserve the extended/diffuse emission, plus to avoid artefacts around bright point sources (see e.g. Traficante et al. 2011; Piazzo et al. 2015). The HiGAL maps have angular beams with a FWHM of about 5, 12, 18, 25, and 36 arcsec at 70, 160, 250, 350, and 500 μm, respectively. And the maps themselves were created with pixel sizes of 3.2, 3.2, 4.5, 6.0, 8.0, and 11.5 arcsec at 70, 160, 250, 350, and 500 μm, respectively.

Molecular CO $J = 1$–0 observations were obtained from the Five College Radio Astronomical Observatory (FCRAO) CO Survey of the Outer Galaxy (Heyer et al. 1998). The angular resolution is 45 arcsec , the velocity resolution 0.127 km s^{-1}, and the rms noise 0.2 K

3 CO EMISSION

Fig. 1 shows a set of images of the CO (1–0) emission distribution within the velocity range from about −11 to 3 km s^{-1} (all velocities are with respect to the local standard of rest, LSR). Each image is an average of the emission in ten consecutive velocity channels, where the corresponding central velocities are indicated in the top side of each box. The velocity range shown was chosen according to the work of Cichowolski et al. (2001), where they found an H I structure related to WR 130 in the velocity range from −10.3 to 1.2 km s^{-1}. To indicate the location of the H II region found by Cichowolski et al. (2001), a 1420 MHz contour delineating it is shown in the top left panel.

As can be seen in Fig. 1 several molecular clouds are present in the area of WR 130. In particular, at −4.65 km s^{-1} the star lies, in projection, inside a well-defined molecular shell. To compare the molecular distribution with the ionized and atomic gas related to WR 130 (Cichowolski et al. 2001), in Fig. 2 the CO emission averaged between −11 and 3 km s^{-1} is shown, along with the 1420 MHz and H I emissions. The left-hand panel of the figure shows the emission distribution at 1420 MHz. The radio continuum emission in the area of WR 130 was extensively analysed by Cichowolski et al. (2001), who concluded that the ring-like feature, named G68.1.1+1.1, is the radio counterpart of the optical region Sh2-98 and it is related to WR 130. On the contrary, based on RRL data, Cichowolski et al. (2001) found that the brightest compact source, named G68.14+0.92, observed at (l, b) = (68.°14, 0.°92) is an H II region located at a distance of about 12 kpc, and thus unrelated to WR 130.

In the middle and right-hand panels of Fig. 2, the CO and H I emissions are shown, respectively, with the radio continuum level delineating the H II region superimposed. From these images it is clear that the ionized gas is surrounded by an atomic shell and that several

Downloaded from https://academic.oup.com/mnras/article-abstract/450/4/3458/992360 by guest on 04 September 2019

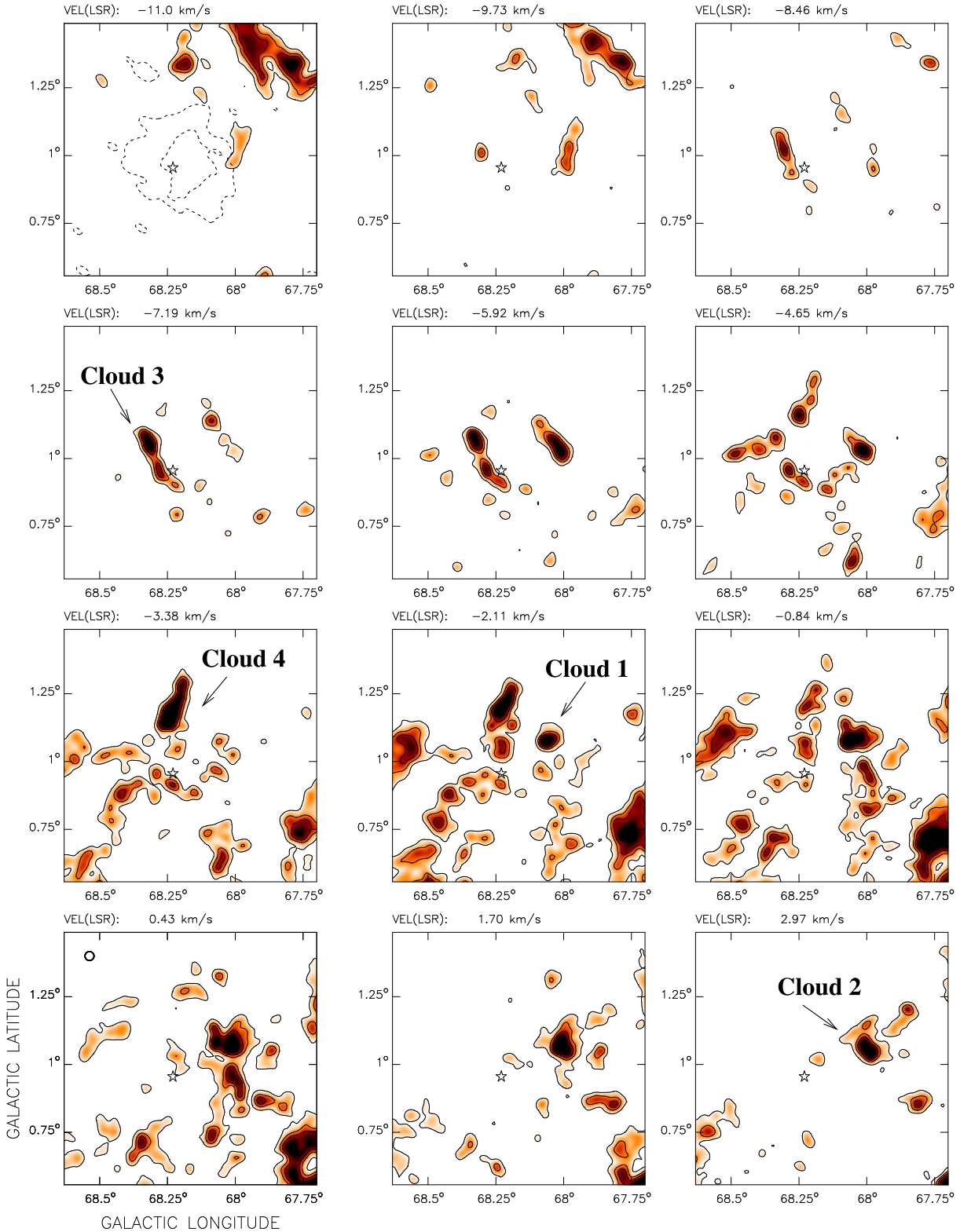

Figure 1. CO emission distribution in the velocity range from −11 to 3 km s^{-1}. Each image is an average of ten consecutive velocity channels, where the corresponding central velocities are indicated in the top side of each box. Contour levels are at 0.3, 0.7, and 1.1 K. Angular resolution is 2 arcmin. Beam shape is shown in the upper left corner of the bottom left panel. The 9.5 K level at 1420 MHz is indicated in the top left panel to delineate the ionized region found to be related to WR 130 by Cichowolski et al. (2001). The star symbol indicates the location of WR 130.

Downloaded from https://academic.oup.com/mnras/article-abstract/450/4/3458/992360 by guest on 04 September 2019

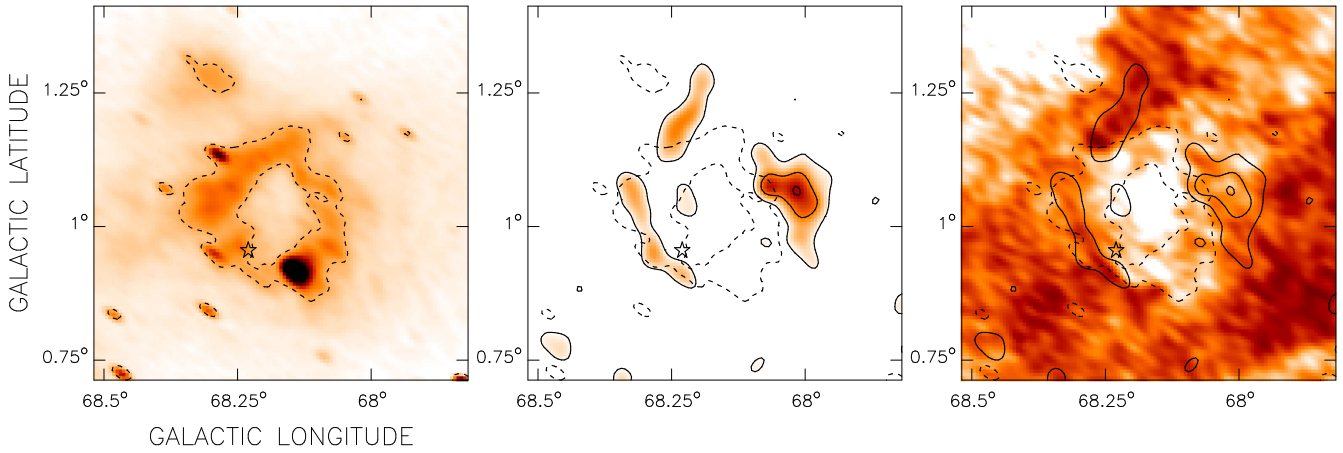

Figure 2. Left-hand panel: CGPS 1420 MHz emission distribution as shown in Cichowolski et al. (2001). Contour level is at 9.5 K. Middle panel: CO emission averaged between −11 and 3 km s^{-1}. Contours levels are at 0.3, 0.7, and 1.1 K. The dotted contour corresponds to the 9.5 K emission at 1420 MHz. Right-hand panel: CGPS H I emission distribution averaged between −10.3 and 1.2 km s^{-1} (as in Cichowolski et al. 2001) with the 1420 MHz and CO contours superimposed. In all the panels the star symbol indicates the location of WR 130.

molecular clouds, which have probably formed part of the molecular cloud where WR 130 was born, are still present. The observed emission distributions clearly indicate that a photodissociated region (PDR) was formed around WR 130.

To estimate the molecular mass of the clouds probably related to WR 130, we first estimate the column density through the empirical relation

$$N(H_2) = X \times I_{CO},$$

where X is the CO-to-H_2 conversion factor, for which we considered the varying relation with the Galactocentric radius R given by Nakanishi & Sofue (2006),

$$X[\mathrm{cm^{-2}\,K^{-1}\,km\,s^{-1}}] = 1.4 \times 10^{20} \exp(R/11\,\mathrm{kpc}),$$

and I_{CO} is the integrated line emission in the velocity range where the cloud is observed, $I_{CO} = \int T\,dv$.

Fig. 2 shows a comparison of the emission observed in the radio continuum at 1420 MHz, the CO and H I emission, the latter two being averages over a few velocity channels. Assuming that the molecular gas shown in Fig. 2 (middle panel) is related to the H I feature found by Cichowolski et al. (2001) as being created by WR 130, we adopt for the molecular clouds the distance inferred by Cichowolski et al. (2001), i.e. $D = 5$ kpc. We thus obtain that the structure is located at $R = 8$ kpc, which yields $X = 2.9 \times 10^{20}$ cm^{-2} K^{-1} km s^{-1}. Then, we estimate the total molecular mass related to WR 130 based on the averaged emission shown in Fig. 2, as well as the mass of the four individual molecular clouds indicated in Fig. 1. These clouds were selected because they host infrared source candidates to be young stellar objects, as will be discussed in Section 5. The molecular masses were derived from $M_\odot = 4.2 \times 10^{-20}\, N(H_2)\, D^2\, A$, where D is the distance in pc and A is the solid angle in steradians. Assuming an elliptical geometry for the individual clouds, the volume density can be estimated as $n(H_2)$ (cm^{-3}) $= 10\,M_\odot/a\,b^2$, where a and b are the major and minor semi-axes, respectively, in pc. The masses and densities obtained, along with the velocity intervals considered for each estimate are shown in Table 1.

We have also estimated the dust masses associated with each cloud, which are given in the last column of Table 1. They were obtained using the *Herschel* data. For each cloud fluxes were measured at 70, 160, 250, 350, and 500 μm by rebinning all the images to the CO resolution and subtracting emission from the local background. Then the spectral energy distribution (SED) of each region was fitted using the models created by DUSTEM (see Section 4) allowing the estimation of the dust masses associated with each region.

The kinetic energy stored in the CO shell can be estimated as $E_{kin} = 0.5\, M_{shell}\, V_{exp}^2$, where V_{exp} is the expansion velocity of the shell and M_{shell} is the total (molecular, atomic, and ionized) shell mass. Adopting an expansion velocity equal to half the velocity interval where the structure is observed, $V_{exp} = 7.0 \pm 1.3$ km s^{-1}, the molecular mass given in Table 1 and the atomic and ionized masses estimated by Cichowolski et al. (2001), 1450 and 3000 $M_\odot$, respectively, we obtain $E_{kin} = (2.5 \pm 1.0) \times 10^{49}$ erg, assuming a 40 per cent error for the masses.. Although Cichowolski et al. (2001) concluded that WR 130 could have alone created the observed structure, it is important to note that they did not take into account the molecular mass present in the shell, which considerably increases the kinetic shell energy. Thus, we can compare now the new value obtained for E_{kin} with the mechanical energy deposited in the ISM by the wind of the WR star, $E_w = (0.7–2.2) \times 10^{50}$ erg (Cichowolski et al. 2001). We obtain $\epsilon = E_{kin}/E_w = 0.007–0.5$. The ratio ϵ measures the energy conversion efficiency in the shell, and according to evolutionary models $\epsilon \leq 0.2$ (Koo & McKee 1992). Thus, not all the possible values of ϵ are compatible with the scenario where the energy injected during the WR phase is enough to create the structure. In this case, the contribution of the energy injected during the O-star phase and/or other massive stars, should be considered. As mentioned in the Introduction, WR 130 is a WNH star, and according to Smith & Conti (2008) its age would be of about 2–3 Myr and its initial mass of at least 60 $M_\odot$. A rough estimation of the energy injected by such a star during its main sequence yields $E_w = (2.5–3.5) \times 10^{50}$ erg (de Jager, Nieuwenhuijzen & van der Hucht 1988), which would be enough to create the observed structure. We have nevertheless looked for the presence of other massive stars in the region. We queried the available catalogues such as the Galactic O-Star Catalog (Maíz Apellániz et al. 2013), the Early-Type Emission-Line Stars Catalogue (Wackerling 1970), the Catalogue of Be stars (Jaschek & Egret 1982), the H-alpha Stars in the Northern Milky Way Catalogue (Kohoutek & Wehmeyer 1997), and the Catalog of Galactic OB Stars (Reed 2003), for early-type and emission stars. No stars were found in any catalogue. The only massive star located nearby is, as mentioned

Downloaded from https://academic.oup.com/mnras/article-abstract/450/4/3458/992360 by guest on 04 September 2019

Table 1. Physical parameters of the molecular gas.

	v_1 (km s^{-1})	v_2 (km s^{-1})	Mass (10^3 M$_\odot$)	Density (10^3 cm^{-3})	Dust mass M$_\odot$
Total	−11	3	46	–	–
Cloud 1	−3.5	1.84	2.2	1.2	114
Cloud 2	−2.35	4.25	4.6	2.4	180
Cloud 3	−10.5	−5.0	2.6	0.8	125
Cloud 4	−7.18	−0.7	6.0	0.8	252

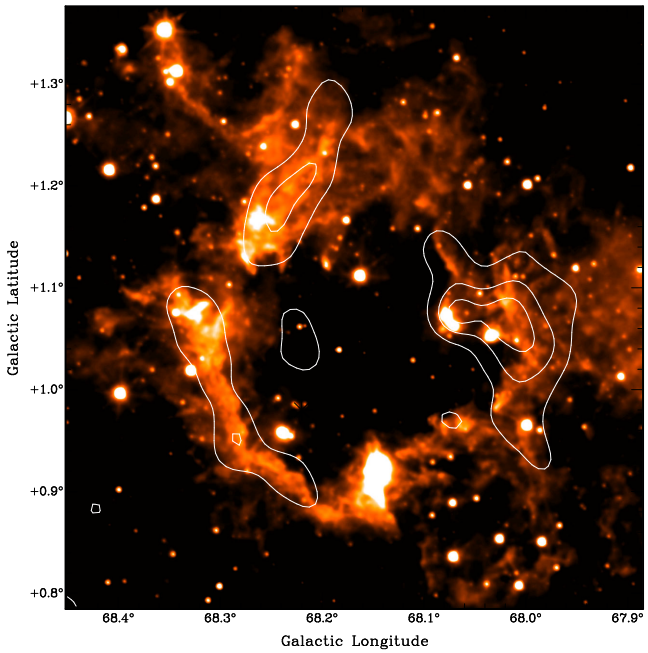

Figure 3. WISE 12 μm image of the region. The contour levels correspond to the averaged CO emission between −11 and 3 km s^{-1} and are at 0.3, 0.6, and 0.9 K.

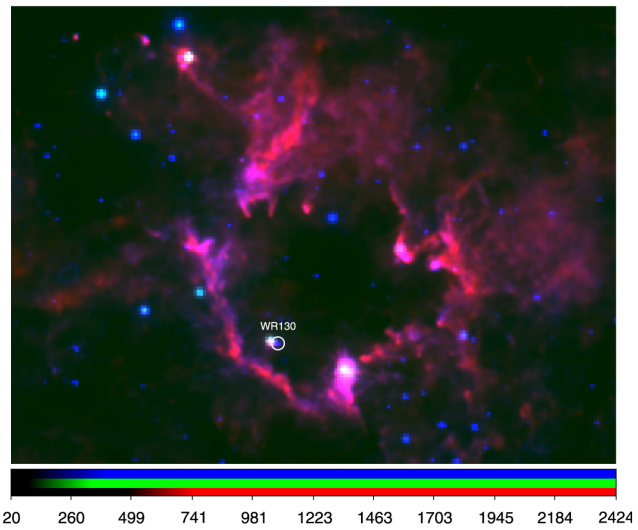

Figure 4. Colour-composite image of the area of WR 130. Blue colour shows the emission at 12 μm (W3 WISE band), green colour represents the emission at 22 μm (W4 WISE band), and red colour shows the emission at 250 μm (SPIRE). The location of WR 130 is indicated by the white circle.

by Cichowolski et al. (2001), an OB star, which has an uncertain spectral type and no distance estimate (Stock, Nassau & Stephenson 1960). It is located in projection not in the centre of the structure but on to the shell (there is a second OB star mentioned by Cichowolski et al. 2001 but its location is actually outside the structure, see fig. 1 of Cichowolski et al. 2001). Although we cannot completely rule out the possibility that the OB star may be playing a role in creating the shell structure, we think that the action of WR 130 is sufficient and most likely dominant in the region.

4 INFRARED EMISSION AND DUST PROPERTIES

In this section, we make use of the *WISE* and *Herschel* data to analyse the distribution of the dust as well as its properties.

As shown in Section 3, the ionized region related to WR 130 is interacting with the molecular gas. As a consequence a PDR is created in the interior layers of the molecular clouds, which can be seen as polycyclic aromatic hydrocarbon (PAH) emission in *WISE A* at 12 μm. Fig. 3 shows that the 12 μm emission displays a cavity surrounded by a roughly thin annular shell emission.

Fig. 4 shows the distribution of the warm and cold dust traced by the 12 μm *W*3 band (PAHs; blue), 22 μm *W*4 band [Very Small Grains (VSGs); green] and *Herschel* 250 μm (big grains; red). Overall the spatial distribution of the three components looks quite similar, at least at the angular resolution of the *WISE* data, 6 and 12 arcsec for *W*3 and *W*4, respectively. The biggest difference takes place on the rim near the WR 130 source itself, where a warmer dust component appears closer to the source, suggesting a more typical photodissociation structure, with the warm gas facing the ionizing source. WR 130 itself, is detected by *WISE* at 12 μm (blue source inside the 1 arcmin radius white circle).

The emission in *Herschel* bands corresponding to 70 (blue), 250 (green), and 500 μm (red) is shown as a colour-composite image in Fig. 5, where several regions of interest can be seen. As can be noticed, the emission observed in the three different bands is similar, in the sense that it forms a shell-like structure, instead of having, as observed in several H II regions, the emission at 70 μm brighter in the interior of the bubble, where the hotter material is expected to be present, and the SPIRE emission, mapping the cooler dust, outside it (e.g. Deharveng et al. 2010; Rodón et al. 2010; Anderson et al. 2012). In this context, the observed large-scale distribution of the infrared emission at the periphery of the ionized gas represents matter accumulated during the expansion of the ionized gas. Additional evidence supporting this conclusion can be seen by comparing the emission distribution among the different infrared bands, as shown in Fig. 6. In this figure, the different lines represent the mean value of the corresponding emission along concentric rings spaced by 1 arcmin and centred at $(l, b) = (68.^\circ17, 1.^\circ035)$. We divided the structure in two halves, the West and East sides, shown in the top and bottom panels of Fig. 6, respectively. The normalized emission was computed by dividing every point by

Downloaded from https://academic.oup.com/mnras/article-abstract/450/4/3458/992360 by guest on 04 September 2019

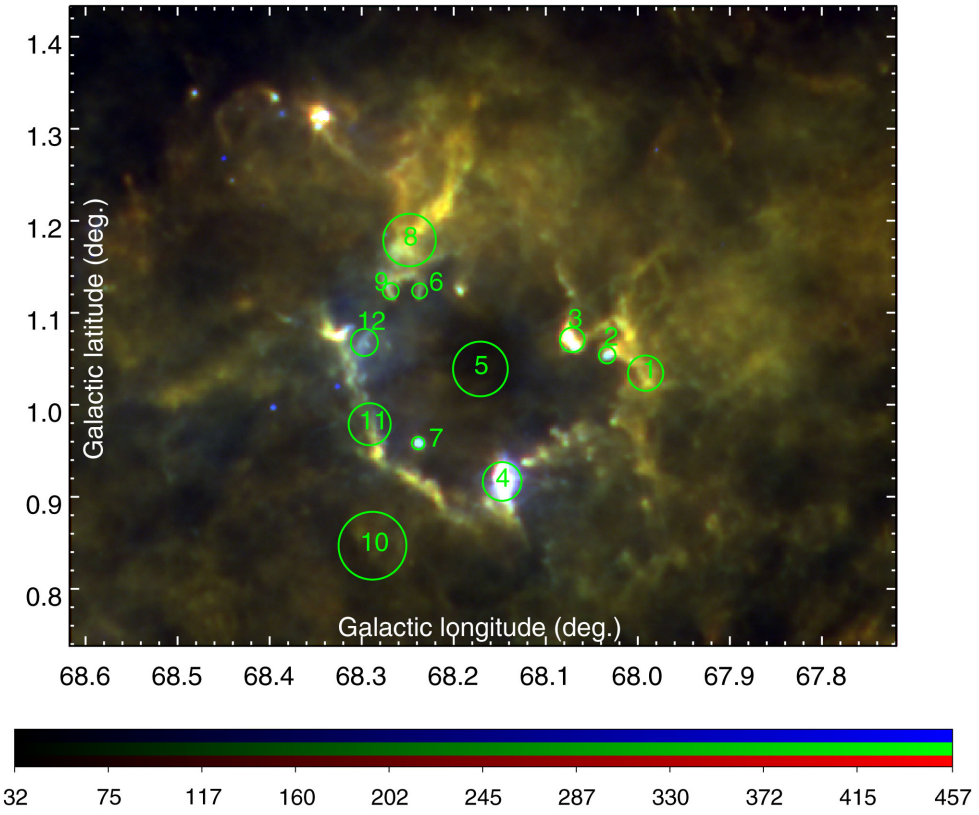

Figure 5. Composite image of the region around WR 130. The image shows SPIRE 500 μm emission in red, SPIRE 250 μm in green and PACS 70 μm in blue. Outlined are the regions where flux densities were estimated.

the corresponding maximum value, 174.5, 215.2, and 39.4 MJy sr^{-1} at 70, 250, and 500 μm respectively, for the East side; and 114.9, 223.1, and 40.2 MJy sr^{-1} for the West half. From this comparison it can be seen that the emissions in the three bands present a similar behaviour and peak together at the location of the shell structure. It can also be noticed that in the West side the emission at 70 μm peaks twice. In this case, the maximum located closer to the centre of the structure is caused by the strong emission observed bordering the molecular cloud labelled as Cloud 1 in Fig. 1.

The fact that the emission distributions show a similar structure at 70 μm and at longer wavelengths such as 500 μm is consistent with the evolutionary path suggested by Smith & Conti (2008) for a WNH star, where, as mentioned in the Introduction of this paper, the energy injected by the WR star impinges directly on to the bubble created during the O-type phase, making it possible that all the dust had been sweep-up into a shell structure. On the other hand, the spatial correlation between the infrared and CO emission is noticeable, suggesting that the infrared emission originated in dense gas, where several CO, ^{13}CO, CH+, and N II transition lines can take place and be responsible for most of the observed emission, as was detected in the area of the H II region Sh2-104 (Rodón et al. 2010). As can be seen in Fig. 3, the dense structure is a fragmented shell of collected material (e.g. Cloud 3) with few probably pre-existing clumps (e.g. Clouds 1 and 4) that clearly distorted the ionization front.

Given that the physical conditions of the structure can be determined from the dust thermal emission, we have selected several regions (see Fig. 5) for which we obtained the cold dust temperature using the estimated *Herschel* fluxes, given in Table 2. To get the flux density in each band, the background, chosen far from the structure, was first subtracted. The regions were selected in order to sample dust related to different parts of the structure, i.e. the interior, the shell, the photodissociation region, the CH II region candidate and cYSOs (see Section 5), and the H II region G68.14+0.92 located at a much larger distance.

The SEDs obtained for the 12 regions, normalized to the 160 μm flux value, are shown in Fig. 7. An inspection of the distributions shows that all regions but three have a similar SED and are therefore expected to contain dust with similar properties. The regions that present a different SED are indicated with different colours and correspond to region 4 (green line), region 5 (red line), and region 7 (orange line). From Fig. 5, it can be seen that region 4 is associated with G68.14+0.92 (the farthest H II region, which is clearly visible in the infrared), region 5 is located in the interior of the shell, and region 7 corresponds to the CH II region candidate (see Section 5).

To characterize the dust located in each region, the SEDs were fitted using the models created by DUSTEM, and a full description of the assumptions and tests performed can be found in the original paper by Compiègne et al. (2011). In a nutshell, DUSTEM creates SEDs of the emission from interstellar dust covering a wavelength range from the mid to far-IR (approximately 3–1000 μm). The emitting dust is the result of three main components: PAHs, amorphous carbon, and amorphous silicates. The abundances and size distribution of each of these components and their interaction with the interstellar radiation field (ISRF), determine essentially the shape of the SED. Roughly, PAHs are expected to dominate the spectra between 3–15 μm, small amorphous carbon grains the 20–40 μm range and larger grains (amorphous carbon and silicates) the longer wavelengths (see e.g. Compiègne et al. 2011, fig. 2). The present version of the code, although it is able to deal with *ISO* and *Spitzer*

Downloaded from https://academic.oup.com/mnras/article-abstract/450/4/3458/992360 by guest on 04 September 2019

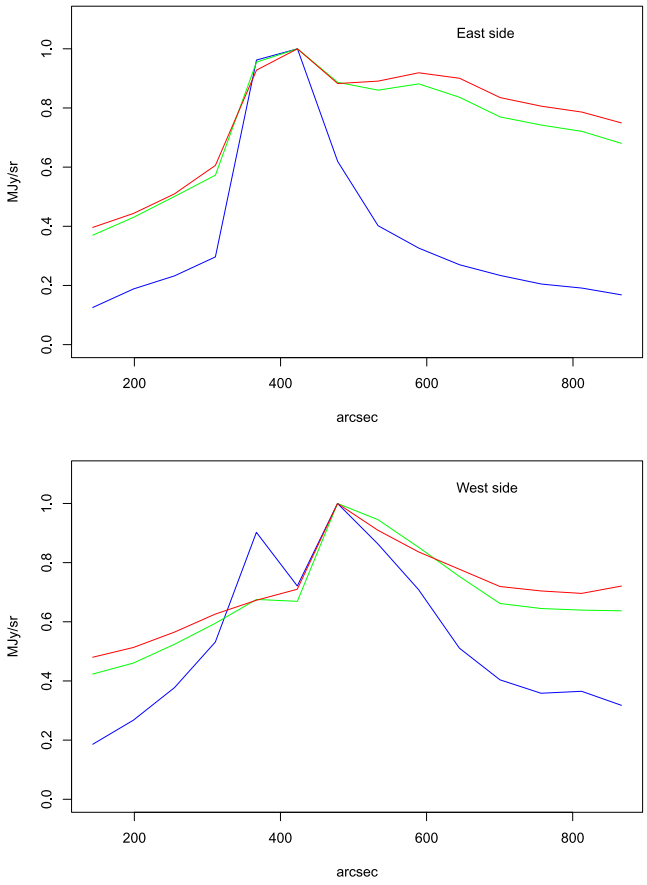

Figure 6. Averaged 70 μm (blue), 250 μm (green), and 500 μm (red) infrared emission distributions as a function of angular distance from the centre of the structure, (l, b) = (68.°17, 1.°035). *Top panel*: East side of the structure. Bottom panel: West side.

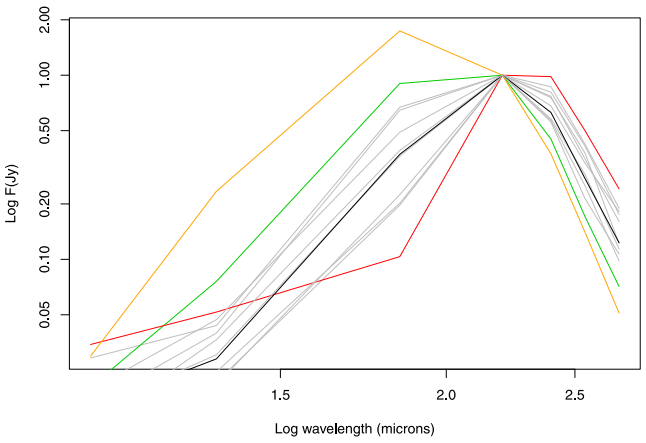

Figure 7. Infrared flux densities measured for the 12 regions shown in Fig. 5 at different wavelengths. The green, red, and orange lines correspond to regions 4, 5, and 7, respectively (see Fig. 5). The black line was taken as the representative infrared energy distribution of the other nine regions (shown in grey).

mid-IR data, needs to be modified to include *WISE* data. Therefore, in this study we are concentrating on the longer wavelength range covered by the *Herschel* Space mission. In terms of determining a dust temperature representative of the medium, the large grains are the ones that can reach a thermal equilibrium with the ISRF, while smaller dust particles are stochastically heated, and therefore, a dust equilibrium temperature is meaningless.

We thus estimated the dust properties of four different regions, the ones mentioned above which present a different SED (see Fig. 7) and region 11 as a reference for the rest of the regions. For each region the models provide the ISRF needed to reach the thermal balance (Mathis, Mezger & Panagia 1983), and the temperatures of the three dust components (small carbon, large carbon, and silicates). All the estimates are shown in Table 3.

As can be seen in Table 3, the estimated temperatures for the H II region G68.14+0.92 and the candidate CH II (see Section 5) are typical for H II regions and higher than the ones found for the shell structure and its interior. On the other hand, the interior region is the coldest, with a temperature around 20 K, which is characteristic of the more diffuse ISM (Boulanger et al. 1996) and consistent with the lack of bubble material in this region. As for the ISRF factor, it can be noted that it is also larger in regions 4 and 7, as expected for regions near a strong radiation field, as is the case for these regions, since they host new stars (see Section 5). On the contrary, for the interior of the shell (region 5) and the shell itself (region 11) the model yields a very low ISRF, suggesting that strong radiations fields are not involved in these regions.

5 YOUNG STELLAR POPULATION

As shown in the previous sections, it is clear that the ISM surrounding WR 130 is strongly affected by the high UV radiation

Table 2. Infrared flux densities estimated for regions 1–12.

			Flux densities (Jy)						
Region	l(deg)	b(deg)	12(μm)	22(μm)	70(μm)	160(μm)	250(μm)	350(μm)	500(μm)
1	67.99	1.03	0.4	0.7	6.4	32.5	26.3	13.4	5.7
2	68.03	1.05	0.6	0.9	13.8	20.6	11.5	4.4	2.2
3	68.07	1.07	0.9	2.2	35.7	55.3	32.1	16.0	6.3
4	68.15	0.92	4.3	16.1	191.3	212.1	95.6	36.2	15.1
5	68.17	1.04	0.2	0.3	0.6	5.8	5.7	2.9	1.4
6	68.24	1.12	0.1	0.2	2.4	6.6	4.5	2.2	1.2
7	68.24	0.96	0.7	5.5	40.9	23.5	8.8	3.3	1.2
8	68.25	1.18	1.3	1.8	19.3	86.0	66.0	30.2	13.8
9	68.27	1.12	0.1	0.3	3.2	8.2	6.2	3.1	1.3
10	68.29	0.85	0.4	0.8	6.6	32.7	28.3	13.8	6.2
11	68.29	0.98	0.6	1.1	14.2	38.2	24.0	10.5	4.7
12	68.30	1.07	0.5	1.2	12.5	25.5	14.5	6.4	2.5

Downloaded from https://academic.oup.com/mnras/article-abstract/450/4/3458/992360 by guest on 04 September 2019

Table 3. Dust properties of the four selected regions.

Region	T_{dust}–small Carbons (K)	T_{dust}– large Carbons (K)	T_{dust}–silicates (K)	ISRF
4 (G68.14+0.92)	34.4	32.5	22.3	8.95
5 (interior)	20.1	19.0	13.7	0.46
7 (CH II)	41.8	39.4	26.6	25.5
11 (shell)	25.5	24.1	17.0	1.72

and mass-loss rate of the star. As proposed by Elmegreen (1998), in this scenario it is highly possible that induced star formation is taking place. With this in mind, we look for primary tracers of stellar formation activity in the area making used of the *IRAS* Point Source Catalogue (Beichman et al. 1988), the MSX Infrared Point Source Catalogue (Egan, Price & Kraemer 2003), the *WISE* All-Sky Source Catalogue (Wright et al. 2010), and a preliminary source extraction from *Herschel* HiGAL data (Molinari et al., in preparation), using the CUTEX source extraction and photometry (Molinari et al. 2011). Within a circular area of 20 arcmin radius, centred at $(l, b) = (68.^{\circ}2, 1.^{\circ}0)$, a total of 29 *IRAS*, 10 MSX (having flux quality $q > 1$ in the four bands), 686 *WISE* (with signal-to-noise ratios greater than seven and photometry flux uncertainties lower than 0.2 mag, in the *W*1, *W*2, and *W*3 bands), sources were found.

To identify the cYSOs among the infrared sources, we adopted the classification scheme described in Junkes, Fuerst & Reich (1992), Lumsden et al. (2002), and Koenig et al. (2012), for the *IRAS*, MSX, and *WISE* data, respectively. For the *Herschel* data, we have used the prescription developed by the HiGAL team (Elia et al. 2013), where essentially a source is considered a candidate YSO if it is detected at 70 μm and appears in at least three contiguous bands.

In this way, we found that two *IRAS* sources, IRAS 19563+3114 and IRAS 19571+3113, are cYSOs. As for the MSX sources, according to the criteria of Lumsden et al. (2002), we have identified massive young stellar object (MYSO) candidates and compact H II region (CH II) candidates. In this region, among the 10 MSX listed sources we found two MYSO and three CH II candidates. We then analysed the listed sources from the *WISE* catalogue and, following Koenig et al. (2012), before attempting to identify the cYSOs, we first selected the non-stellar sources, such as PAH-emitting galaxies, broad-line active galactic nuclei (AGNs), unresolved knots of shock emission, and PAH-emission features. A total of 119 sources were dropped from the list, and among the remaining 567 only two were identified as Class I sources (e.g. sources where the IR emission arises mainly from a dense infalling envelope) and nine as Class II sources (e.g. sources where the IR emission is dominated by the presence of an optically thick circumstellar disc). In Fig. 8, we show the $(W2 - W3)$ versus $(W1 - W2)$ colour–colour diagram for all the uncontaminated sources, where the Class I and Class II sources are shown in red and green, respectively. Given that protostellar objects with intermediate/high masses can be identified among the Class I sources by additionally requiring that the magnitude $W3 < 5$ (Higuchi et al. 2013), and that neither of the detected two Class I sources satisfies this criterion, it seems that both are low-mass protostars.

In the far-infrared, using the *Herschel* data, one is systematically detecting more deeply embedded objects; although is clear that those less embedded are likely to be detected at shorter wavelengths as well. Unlike low-mass protostars where there is a general agreement on their classification as function of their SED and evolutionary stage, from Class 0 to Class III, indicating their age and the clearance of their protostellar envelope (see e.g. Evans et al. 2009),

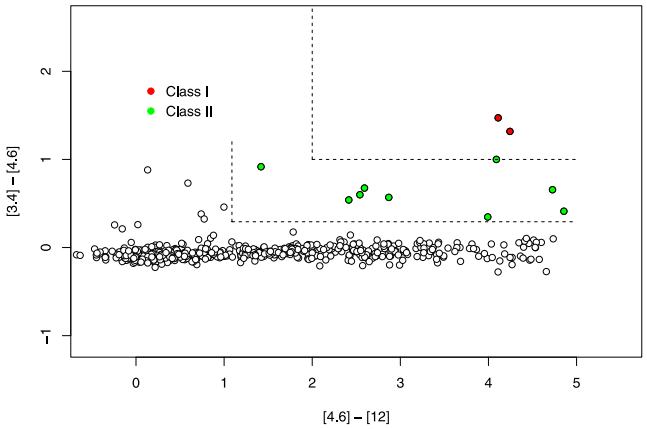

Figure 8. *WISE* colour–colour diagram showing the areas where the Class I and Class II YSO candidates are located according to the Koenig et al. (2012) criteria.

for massive YSOs is not the case. It is possible, however, under the 'mass accretion paradigm' of massive star formation (see e.g. Tan et al. 2014, and references therein), to develop a similar scheme where the youngest more embedded massive YSOs are identified as Class 0 and so on (Molinari et al. 2008). Observationally, the HiGAL team has developed a method to select YSO 'candidates' that allows such classification and places the sources in a bolometric luminosity versus mass envelope diagram, providing an idea on their evolutionary stage. The scheme, as mentioned above, requires a detection at 70 μm and three contiguous bands (to create a SED); for further details see Elia et al. (2013). In this study, we have used such scheme, but we have gone a step further by trying to fit a SED model to data when possible, and using the Robitaille–Whitney *Hyperion* grid of models for such task (Robitaille & Whitney 2014).

The location of all the cYSOs found are indicated in Fig. 9 and their infrared properties listed in Table 4. From Fig. 9, it is evident that star formation is taking place in the local environment of WR 130, and that the cYSOs are found preferentially on to the molecular clouds labelled as Cloud 1, 2, 3, and 4, in Fig. 1. It is clear that the spatial distribution of the cYSOs follows the distribution of the high-column density matter.

As can be noticed, the *IRAS* source IRAS 19571+3113 (# 2 in Table 4), two MSX sources (#4 and #7), and nine *Herschel* sources (#28 to #36) are located on to the H II region G68.14+0.92, which, as pointed out by Cichowolski et al. (2001), is not related to WR 130. Moreover, Bronfman, Nyman & May (1996) in their survey of the CS(2-1) emission towards *IRAS* point sources in the Galactic plane, observed, in direction to IRAS 19571+3113, CS(2–1) emission at –62.6 km s^{-1}, suggesting that a high-density molecular clump is associated with G68.14+0.92 and may harbour new stars. Given that this region is far away from the area under study, these 12 infrared sources will not be considered further.

As regards to the MSX source candidate to be a CH II G068.2383+00.9596 (# 5 in Table 4), it coincides with the *Her-*

Downloaded from https://academic.oup.com/mnras/article-abstract/450/4/3458/992360 by guest on 04 September 2019

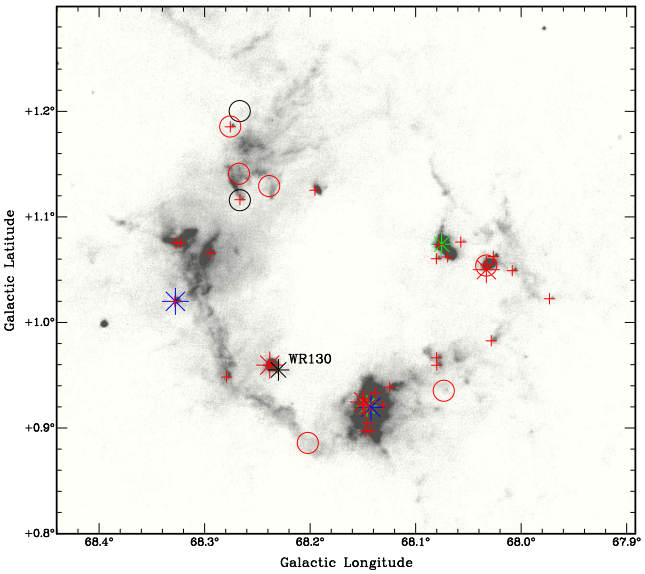

Figure 9. *Herschel* image at 70 μm with the location of the cYSOs superimposed. Green, blue, and red asterisks correspond to *IRAS* YSO, MYSO, and CH II candidates, respectively, while black and red circles indicate the location of *WISE* Class I and Class II candidate sources, respectively. *Herschel* sources are indicated by red crosses.

schel source #38 and, from Fig. 9, it can be seen that, in projection, their location is very close to WR 130. This source is observed both at radio and infrared wavelengths and it is included in the Red MSX Source (RMS) survey (Urquhart et al. 2008). According to these authors, G068.2383+00.9596 is associated with the infrared source IRAS 19572+3119, several 2MASS point sources, the *WISE* source 5087 (with estimated flux values only at 12 and 22 μm), and the radio source G068.2389+00.9592 (Urquhart et al. 2009), for which a flux intensity of 6.1 mJy is given at 5 GHz. On the other hand, Urquhart et al. (2011) detect neither ammonia nor water maser emission in the direction to this infrared source, and cannot thus suggest any kinematical distance to it. An inspection of the CO data cube shows, however, that CO emission in this direction is only detected at about -62 km s^{-1}, as shown in Fig. 10, suggesting a further distance for the CH II candidate, of about 12 kpc, similar to the distance of the H II region G68.14+0.92, indicating that we have located an active star formation region that is located far beyond the solar circle. In this case, the infrared sources #5 and #38 cannot be associated with WR 130. On the other hand, an inspection of the entire CO data cube reveals that sources #13 and #15 (see Table 4) are not immersed in any molecular cloud, indicating that, if they are YSOs, either they have already moved away from the place where they were formed or that they dissipated it.

From the remaining cYSOS appearing in Table 4, it is important to mention that CO emission in their direction is only observed at the radial velocity interval between -9 and -15 km s^{-1}, coincident with the radial velocity of the molecular structure, suggesting an association between them and the molecular clouds. The exceptions are Source #8, for which CO emission is also detected at -60 km s^{-1} and Sources #22 and #26, in which direction there is CO emission also at $\sim-$ 40 km s^{-1}.

Among the cYSOs, two groups of sources are of particular interest. As can be seen from Fig. 9, four sources, #1-23 (since sources #1 and #23 spatially coincide), #21, #22, and #26 are seen projected on the periphery of the CO cloud named as Cloud 1 in Fig. 1, while three sources, #3-12-20, #17, and #18, are located on to Cloud 2. In both cases, the cYSOs are located on the side nearly facing the star WR 130. This suggests that they could be bright-rimmed clouds (e.g. Morgan, Urquhart & Thompson 2009) being excited by the ionizing radiation from WR 130, in which case one could expect to find a radio continuum counterpart (e.g. Schwartz 1985). An inspection of Fig. 11 shows indeed the presence of a weak radio continuum source possibly barely resolved (it is hard to clearly separate it from its surrounding emission) with the CGPS beam, thus suggesting a size of approximately 1 arcmin or less. A peak 1420 MHz flux density of $\sim 10 \pm 1$ mJy is obtained with an estimated total flux density of 18 ± 3 mJy in the border of Cloud 1 and a peak flux value of about 2 mJy is estimated for the emission bordering Cloud 2.

Assuming the radio continuum emission to be free–free emission, we can use the models of Mezger & Henderson (1967) to infer the properties of the ionized gas, following the procedure outlined by Pineault (1998). Since we do not know a priori the actual distribution of the gas, we take the simplest possible model for the source, namely that of a sphere with constant density.

Then the electron density n_e, mass of ionized gas M and total number N_u of UV ionizing photons per second (e.g. Chaisson 1976) are given by

$$n_e = 6.35 \times 10^2 \, u_1 \, a^{-1/2} \, T_4^{0.175} \, \nu_{GHz}^{0.05} \, S_\nu^{0.5} \, \theta_{Ga}^{-1.5} \, D_{kpc}^{-0.5} \, \mathrm{cm}^{-3},$$

$$M/\mathrm{M}_\odot = 0.386 \, u_2 \, a^{-1/2} \, T_4^{0.175} \, \nu_{GHz}^{0.05} \, S_\nu^{0.5} \, \theta_{Ga}^{1.5} \, D_{kpc}^{2.5},$$

$$N_u = 0.76 \times 10^{47} \; T_4^{-0.35} \, \nu_{GHz}^{0.1} \, S_\nu \; {D_{kpc}}^2 \, \mathrm{s}^{-1},$$

where S_ν is the measured flux density in Jy, θ_{Ga} the measured half-power width in minutes of arc, T_4 the electron temperature in units of 10^4 K, $a(\nu, T_e)$ the Gaunt factor (of order unity), D_{kpc} the distance in kpc and ν_{GHz} the frequency in GHz. The parameters u_1 and u_2 are of order unity for a spherical source model. As the observing frequency appears with a very low exponent, all frequency factors are also of order unity. Assuming a distance of 5 kpc (Cichowolski et al. 2001), a temperature of 10^4 K and using $\theta_{Ga} \sim 1$ (valid for a source unresolved with a beam of the order of 1 arcmin), the above three equations thus simplify to

$$n_e \sim 290 \, S_\nu^{0.5} \, \mathrm{cm}^{-3},$$

$$\mathrm{M/M}_\odot \sim 22 \, S_\nu^{0.5},$$

$$N_u \sim 1.9 \times 10^{48} \, S_\nu \; \mathrm{s}^{-1}.$$

It should be emphasized at this point that the above estimate for n_e is likely an underestimate since the source geometry is that of a thin layer of ionized gas on the star-facing side of the cloud. Since the electron number density is of the form $n_e \propto \theta_{Ga}^{-1.5} \propto (\mathrm{volume})^{-1/2}$, we expect n_e to scale roughly as $\eta^{-1/2}$ if we assume the thickness of the layer to be given by η times the cloud radius.

Using the measured peak flux density of 10 and 2 mJy for the border of Cloud 1 and 2, respectively, the above numbers reduce to the values given in Table 5. As both sources are essentially unresolved at 1 arcmin, the estimated densities and ionized masses are a lower and upper limit, respectively. Their corresponding maximum size is of the order of 1.5 pc for a distance of 5 kpc.

Assuming that WR 130 is the star providing the ionizing radiation, which van der Hucht (2001) gives as $N_{WR} = 5.0 \times 10^{48}$ s^{-1}, we can calculate the number of ionizing photons N_{WR}^i intercepted by the radio continuum features bordering Cloud 1 and 2. For this estimate, we considered that the border of Cloud 1 is located some 12 arcmin or 17.4 pc from WR 130 (we do not make any correction to the distance or cloud size due to projection effects as these

Downloaded from https://academic.oup.com/mnras/article-abstract/450/4/3458/992360 by guest on 04 September 2019

Table 4. *IRAS*, MSX, *WISE* and *Herschel* sources found to be YSO candidates.

			IRAS sources				
#	Designation	(*l*, *b*)	F_{12}[Jy] (Q_{12})	F_{25}[Jy] (Q_{25})	F_{60}[Jy] (Q_{60})	F_{100}[Jy] (Q_{100})	Notes
1	19563+3114	68.07, 1.07	1.690 (3)	4.411 (3)	56.06 (3)	105.2 (2)	Cloud 1
2	19571+3113	68.146, 0.92	3.682 (1: upper limit)	15.050 (2)	173.80 (3)	399.9 (2)	G68.14+0.92
			MSX sources				
#	Designation	(*l*, *b*)	F_8[Jy] (Q_8)	F_{12}[Jy] (Q_{12})	F_{14}[Jy] (Q_{14})	F_{21}[Jy] (Q_{21})	Notes
3	G068.0331+01.0543	68.03, 1.05	0.74 298 (4)	1.3394 (1)	0.85 034 (1)	2.7624 (1)	CH II, Cloud 2
4	G068.1492+00.9247	68.149, 0.92	1.08 850 (4)	1.9132 (3)	1.42 180 (3)	3.0316 (3)	CH II, G68.14+0.92
5	G068.2383+00.9596	68.238, 0.9596	0.96 607(4)	1.4840 (3)	1.47 640 (3)	8.0493 (4)	CH II, CO also at -62 km s^{-1}
6	G068.3277+01.0201	68.32+01.02	0.60 381 (4)	2.30 430 (4)	2.8046 (4)	4.9903 (4)	MYSO, Cloud 3
7	G068.1424+00.9197	68.14, 0.919	0.37 255 (4)	0.69 779 (1)	1.2673 (3)	3.4386 (3)	MYSO, G68.14+0.92
			WISE sources				
#	Designation	(*l*, *b*)	*W*1 [mag]	*W*2 [mag]	*W*3 [mag]	*W*4 [mag]	Notes
8	J195819.33+313643.5	68.266, 1.20	14.366	12.894	8.784	7.292	Class I, Cloud 4, CO also at -60 km s^{-1}
9	J195839.60+313404.4	68.266, 1.11	13.436	12.118	7.874	5.252	Class I, Cloud 4
10	J195824.18+313643.7	68.27, 1.185	9.115	8.575	6.160	3.996	Class II, Cloud 4
11	J195833.72+313453.6	68.267, 1.140	11.840	11.493	7.501	5.581	Class II, Cloud 4
12	J195820.08+312011.3	68.033, 1.053	9.388	8.388	4.298	2.370	Class II, Cloud 2
13	J195925.21+312333.1	68.20, 0.88	14.019	13.607	8.751	7.244	Class II, no CO
14	J195832.30+313304.2	68.238, 1.129	13.383	12.727	8.000	5.588	Class II, Cloud 4
15	J195854.39+311831.1	68.073, 0.935	10.025	9.456	6.587	4.210	Class II, no CO
			Herschel sources				
#	Designation	(*l*, *b*)	F_{70} [Jy]	F_{160} [Jy]	F_{250} [Jy]	F_{350} [Jy]	F_{500} [Jy]
16	238687	67.973, 1.022	0.329	0.761	1.611	–	–
17	238749	68.008, 1.049	0.785	1.689	5.746	4.558	2.004
18	238786	68.026, 1.062	1.3	2.864	6.511	12.94	2.957
19	238789	68.028, 0.983	1.276	5.812	5.762	3.265	1.663
20	238797	68.033, 1.054	11.424	16.491	12.655	2.347	2.293
21	238835	68.057, 1.076	0.455	3.849	6.204	–	–
22	238863	68.069, 1.062	15.427	20.963	13.061	10.912	6.197
23	238880	68.078, 1.074	74.122	49.372	36.245	18.919	9.604
24	238886	68.08, 0.959	0.804	3.267	2.641	1.705	2.219
25	238887	68.08, 0.966	0.891	2.022	4.1	–	–
26	238888	68.080, 1.06	1.053	3.049	1.564	–	–
27	238953	68.124, 0.939	1.478	4.173	3.185	5.83	2.375
28	238963	68.130, 0.921	0.551	1.354	2.001	–	–
29	238979	68.138, 0.933	2.115	3.978	1.344	–	–
30	238993	68.143, 0.897	8.92	14.102	13.491	0.501	–
31	239001	68.145, 0.905	1.717	10.201	6.913	12.91	6.887
32	239003	68.146, 0.922	5.407	27.825	–	–	–
33	239007	68.148, 0.897	1.284	3.301	–	–	–
34	239008	68.148, 0.915	3.876	3.983	16.76	–	–
35	239012	68.150, 0.928	16.703	70.192	35.56	–	–
36	239013	68.150, 0.922	8.439	46.275	35.76	21.896	11.192
37	239094	68.195, 1.125	2.781	13.222	9.275	4.634	2.413
38	239192	68.24, 0.959	37.411	18.088	15.479	5.295	2.463
39	239252	68.266, 1.116	1.249	4.231	2.361	–	–
40	239271	68.276, 1.185	0.955	1.444	1.758	0.639	–
41	239279	68.279, 0.948	0.739	6.536	12.99	8.077	4.812
42	239302	68.294, 1.065	0.73	1.843	6.333	1.531	1.218
43	239366	68.323, 1.076	1.567	13.42	7.726	11.75	4.159
44	239370	68.327, 1.075	5.431	11.735	16.903	–	–
45	239371	68.328, 1.02	4.212	0.872	0.808	–	–

cancel out), and the border of Cloud 2 is a little bit further from WR 130, at about 12.5 arcmin or 18 pc. We find that a fraction $f1 \sim 0.006$ and $f2 \sim 0.007$ of the photons from WR 130 would be intercepted for each cloud, so that $N^{i1}_{\rm WR} \sim 3.0 \times 10^{46}$ s^{-1} and $N^{i3}_{\rm WR} \sim 3.5 \times 10^{46}$ s^{-1}. It would seem, at least at first sight, that WR 130 alone is sufficient to power the observed radio continuum emission.

We thus have two molecular clouds, labelled Cloud 1 and 2, presenting a bright rim and each harbouring cYSOs. This together with the fact that the observed cometary shapes of the bright rims are quite apparent with their tips pointed towards the location of WR 130 (see Fig. 9) suggest the possibility that the cYSOs were formed under the radiative driven implosion (RDI) mechanism (Bertoldi 1989). This mechanism takes place when a photoionization shock is driven

Downloaded from https://academic.oup.com/mnras/article-abstract/450/4/3458/992360 by guest on 04 September 2019

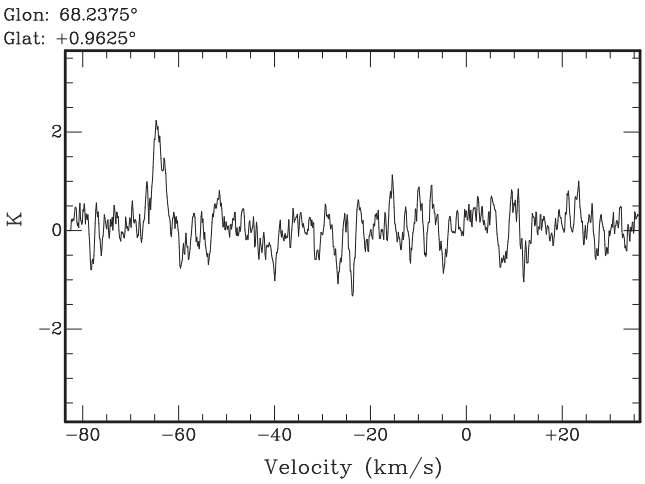

Figure 10. CO emission in direction to the MSX source G068.2383+00.9596.

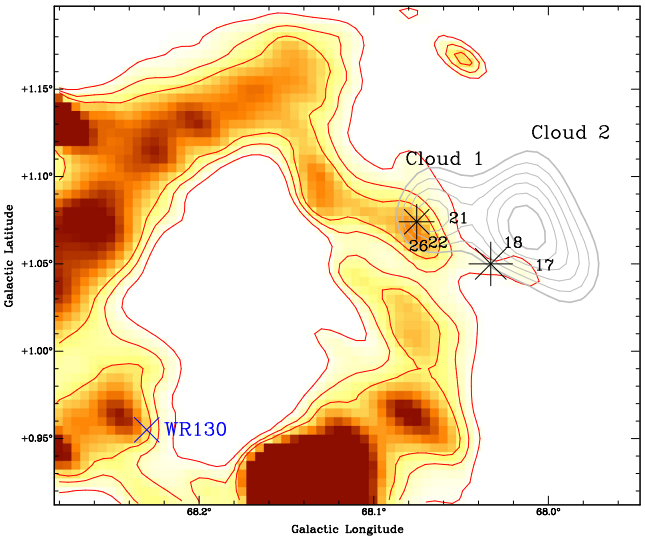

Figure 11. 1420 MHz emission distribution in the area of sources #1-23 and #3-12-20 (both indicated by black asterisks). Red contours are at 9.2, 9.6, and 10 K. Black contours correspond to the averaged CO emission between −2.35 and 4.25 km s^{-1}, from 1 to 2 K with a step of 0.2 K. The location of WR 130 is indicated by the blue cross. *Herschel* cYSOs are indicated by their source numbers (see Table 4).

into the molecular gas. To ascertain whether this is the case, it is necessary to compare the pressure of the ionized layer bordering the molecular cloud with the molecular pressure. If the cloud is underpressured with respect to the ionized layer or the pressures are similar, the ionization front will be able to propagate into the cloud and then modify its evolution (Lefloch & Lazareff 1994).

The pressure in the ionized boundary layer can be evaluated from the electron density as $P_i = 2\,\rho_i\,c_i^2$, where ρ_i is the density in the boundary layer, $\rho_i = n_e\,m_H$ and c_i is the sound speed in the ionized gas ($c_i \sim 11.4$ km s^{-1}). As mentioned above, this pressure should be compared with the pressure of the molecular cloud, which can be estimated, assuming that the thermal component can be neglected, from the turbulent velocity dispersion, σ^2, and the molecular density, ρ_m, as $P_m = \sigma^2\,\rho_m$, where σ^2 may be written as $\sigma^2 = \Delta\,v^2/(8\ln 2)$, $\Delta\,v$ being the observed velocity line width of the molecular cloud gas. The results are given in Table 5. Before comparing the obtained values it is important to mention that the errors involved in these estimates are large. As mentioned before, the electron densities obtained for the ionized gas are lower limits, and thus the estimates of P_i are also underestimates. On the other hand, since the molecular pressure depends on the geometry adopted to estimate the molecular density, the CO-to-H_2 conversion factor X, and the distance adopted for the structure, its value has at least a 60 per cent error. Bearing this in mind, from Table 5 we can see that the pressures P_i and P_m obtained for Cloud 1 are similar while in the case of Cloud 2 the molecular pressure is higher than the pressure of the ionized gas, suggesting that the shock could not yet affect the molecular gas. However, given the large errors involved in the estimates, with the data at hand we cannot completely rule out the possibility that the shock front has already penetrated into Cloud 2.

The second group of sources of interest in Fig. 9 is located on to Cloud 4 (see Fig. 1). This group consists of five *WISE* sources (two of them coincide with *Herschel* sources), two classified as Class I YSOs and three as more evolved, Class II, objects (see Table 4). An inspection of Fig. 4 clearly shows, more strikingly at 250 μm, two jet-like features spatially coincident with the border of molecular Cloud 4. Moreover, two of the cYSO, identified as sources #9 and #39 and #14 in Table 4, are located on to the tip of these structures. A close-up of this region is shown in Fig. 12. The cometary shape of the infrared structures suggests that the RDI mechanism could be at work in this molecular cloud, but the low angular resolution of both the molecular and radio continuum data prevents carrying out the analysis in this region.

Among the rest of the cYSOs presented in Table 4, it can be seen that four sources (#6-45, #42, #43, and #44) are located on to Cloud 3 (see Fig. 1), while the rest are distributed on to the general CO shell structure.

5.1 Physical properties of cYSOs

To characterize the cYSOs identified located in projection on to the molecular clouds, we constructed their SED using the grid of models and fitting tools of Robitaille et al. (2006, 2007). The SED fitting tool fits the data allowing the distance and external foreground extinction as free parameters. We gave a distance range of 4.5–5.5 kpc. The visual absorption range for each source was set making use of the H I and CO data cubes to estimate their column densities at the distance of the structure, using the relation N(H I) + 2 N(H_2) ∼1.9 × $10^{21} A_V$ (Bohlin, Savage & Drake 1978), where N(H I) is the H I column density and is given by N(H I)(cm^{-2}) = 1.824 × 10^{18} T(K) Δv (km s^{-1}), and N(H_2) is the molecular column density, given by N(H_2)(cm^{-2}) = 2.3 × 10^{20} T (K) Δv (km s^{-1}), where, in both cases, T is the brightness temperature and Δv is the velocity interval between the structure and the

Table 5. Estimated parameters for the boundary ionized layers related to Clouds 1 and 2.

Cloud	n_e (cm^{-3})	M_i ($M_\odot$)	N_u (10^{46} s^{-1})	N^i_{WR} (10^{46} s^{-1})	P_i/k (10^6 cm^{-3} K)	P_m/k (10^6 cm^{-3} K)
1	29	2.2	2.0	3.0	1.9	2.0
2	12	1	0.4	3.5	0.6	6

Downloaded from https://academic.oup.com/mnras/article-abstract/450/4/3458/992360 by guest on 04 September 2019

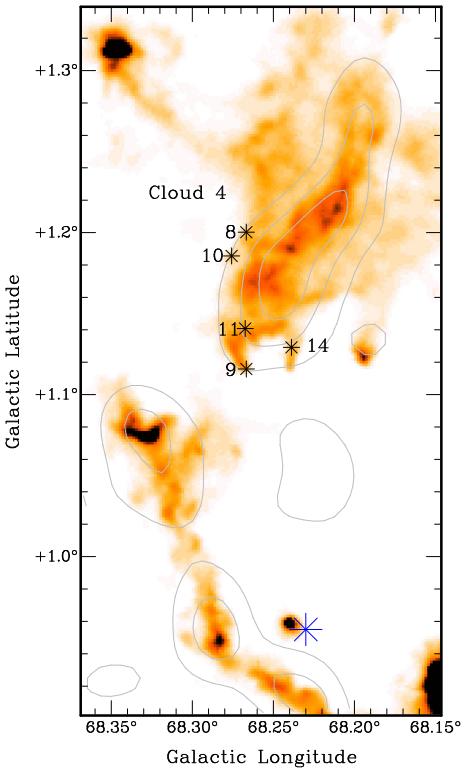

Figure 12. 250 μm emission distribution in the area of the molecular Cloud 4. The five *WISE* sources located on to this cloud are indicated with asterisks and with their corresponding numbers (see Table 4). Grey contours are from 0.4 to 1.6 K with a step of 0.4 K and correspond to the averaged CO emission between −7.18 and −0.7 km s^{-1}. The location of WR 130 is indicated by the blue asterisk.

observer. The adopted range for each source is given in the last column of Table 6.

For each cYSO besides using the photometry given in Table 4, we search their counterpart in other infrared ranges, to use in the fitting as many points as possible to better constrain the estimated parameters. Thus, for sources #3-12-20, #11, #14, and #15, *JHK* photometry was obtained from the 2MASS catalogue. For source #1-23 the flux given in the MSX catalogue at Band *A* was also considered. For source #3-12-20 out of the four MSX bands observed only Band *A* was considered due to the bad quality of the other three, and the *IRAS* fluxes obtained from the *IRAS* catalogue were used as upper limits.

For each source, based on all the fitted models satisfying $\chi^2 - \chi^2_{\rm best} < 2\,N$, where $\chi^2_{\rm best}$ is the goodness-of-fit parameter for the best-fitting model and N is the number of input observational data points, we estimated some parameters such as the stellar mass, stellar temperature, stellar age, envelope accretion rate, envelope mass, and total source luminosity. To estimate the parameters, we carefully inspect every distribution considering all the models that satisfy the criteria mentioned above. The results are listed in Table 6. We note that, with the data at hand, even when the data points can be fitted with great goodness, just a few parameters are well constrained and in some cases only lower and/or upper limit values can be given.

As can be seen in Table 6 all the sources but five are in a very early stage of their formation, with ages lower than 10^5 yr, still having high envelope masses, of the order of hundreds, and envelope accretion rates of the order of 10^{-5}–10^{-3} M$_\odot$ yr^{-1}. Similarly, most of the cYSOs have low/intermediate masses, lower than 7 M$_\odot$, although these values will probably increase considerably since they are still accreting lot of mass from their envelopes.

As mentioned before, Fig. 9 shows that sources #1-23, #21, #22, and #26 are located within the molecular Cloud 1, while sources #3-12-20, #17, and #18 are within Cloud 2. An inspection of the ages

Table 6. SED parameters obtained for the cYSOs.

#	Stellar mass (M$_\odot$)	Stellar temperature (K)	Stellar age (10^3 yr)	Envelope mass (M$_\odot$)	Envelope accretion rate (M$_\odot$ yr^{-1})	Total luminosity (10^3 L$_\odot$)	A_V (mag)
1-23	8	4130	1.3	476	5.6×10^{-4}	2.5	4–10
3-12-20	4	4143	1.7	20	0.002	0.3	4–8
6-45	6.8	4435	21	0.4	3.7×10^{-5}	0.9	2–5
8	3–6	11 000–18 700	>1200	$<7 \times 10^{-7}$	0	0.05–0.97	2–4
9-39	1.2	3967 ± 15	1.1–1.3	69–72	$(0.4 \pm 0.1) \times 10^{-4}$	0.04–0.05	2–6
10-40	4.6	11270	836	10.6	1.5×10^{-7}	0.4	3–7
11	5.3 ± 0.4	4688±118	95–185	8–13	$(0.3–1.0) \times 10^{-4}$	0.1–0.2	2–6
13	4.2 ±0.3	14 855±600	2200–4100	$<9 \times 10^{-8}$	0	0.26±0.06	2–6
14	1.9	4320	112	12	9×10^{-5}	36	2–7
15	3.5	11820	1954	10^{-8}	0	0.2	2–4
16	1.3 ± 0.3	4092 ± 94	7–14	97 ± 17	$(50 \pm 7) \times 10^{-5}$	0.03 ± 0.01	5–8
17	3.4	4390	39	251	10^{-3}	0.09	6–9
18	5.5	4433	28	760	2×10^{-3}	0.2	7–10
19	5.5	4433	28	760	2×10^{-3}	0.2	4–7
21	2.6	4200	7.6	274	10^{-3}	0.1	6–9
22	2.3–2.5	4215 ± 22	8–15	223–274	10^{-3}	0-07–0.10	6–9
24	2.3–3.4	4200–4393	6.4–38.7	223–345	10^{-3}	71–112	4–7
25	1.6–3.4	4114–4393	6–39	165–251	10^{-3}	0.05–0-09	4–7
26	2.5 ± 0.8	4254 ± 125	23 ± 9	14–262	$(7 \pm 2) \times 10^{-4}$	0.08 ± 0.02	4–8
27	5.5	4433	28	760	2×10^{-3}	0.2	3–5
37	4.9	4380	6–20	540–840	2×10^{-3}	0.25–0.30	4–6
41	4.6	4208	4.7	1241	2×10^{-3}	0.3	5–8
42	2.3–3.4	4200–4393	7.6–38.8	223–274	10^{-3}	0.07–0.10	2–5
43	4.6	4208	4.7	1241	2×10^{-3}	0.3	5–8
44	4.6–8.1	4423 ± 189	< 30	1142 ± 228	2×10^{-3}	0.5 ± 0.2	5–8

Downloaded from https://academic.oup.com/mnras/article-abstract/450/4/3458/992360 by guest on 04 September 2019

estimated for these cYSOs shows that in Cloud 1 the age gradient is as expected for sources #1-23, #22, and #26, if the RDI mechanism took place in this cloud, in the sense that the oldest source (#26, among these three) is located closest (in projection) to the WR star, then is source #22 and then #1-23. The problem is with source #21, which, since it is located further from WR 130 should be younger. A similar situation occurs for the three sources located within Cloud 2, where the ages of sources #17 and #18 are larger than the one of #3-12-20. Looking at the SEDs fitting we found that for these three sources particulary the fitting is not satisfactory. More data at other wavelengths would be useful to better estimate the age of these sources.

Three of the sources that have higher ages are sources #8, #10-40, and #11, all lying in projection on to Cloud 4. In this case, if the RDI mechanism is responsible for the star formation in the cloud, given the location of these three cYSOs with respect to WR 130, they would have the lowest ages. Since this is not what we obtained, we suggest that either another mechanism is acting in Cloud 4 or that both sources are not related to this cloud. As mentioned before, CO emission is also detected at -60 km s^{-1} in direction to source #8. Also sources #13 and #15 are among the oldest cYSOs, which is consistent with the fact that, as mentioned before, they are not immersed in any molecular gas.

The simultaneous presence of envelope-dominated YSOs (typical age around 10^4 years) and a WR star in the same region suggests that different episodes of star formation have occurred in the region. Since WR 130 is an evolved star, we can speculate that the formation of young sources in the region might have been triggered by the expanding bubble.

6 SUMMARY

The previous observations by Cichowolski et al. (2001) and those reported here allow us to describe a consistent picture of the recent evolution of WR 130 and of its effect on its immediate environment on large as well as small scales. The initial results of Cichowolski et al. (2001) showed that the continuum radio emission and H I kinematical analysis were in total agreement with the generally accepted picture of stellar wind evolution (e.g. Castor et al. 1975; Weaver et al. 1977). In this paper, we have gone one step further and used recent high-quality IR and CO data to study for the first time the molecular and dust properties of the ISM local to this WR star.

The time-scales involved are consistent with the wind of the O-star phase having formed an initial cavity in the surrounding ISM. The wind of the star now in its WR phase seems to be interacting directly with the cavity wall as there is no sign of massive ejection having taken place in the recent history of the star. If any such ejection took place, it is likely to have been a minor event. In all probability WR 130 is now in a pre-LBV phase.

On large scales, an inspection of the CO data cube reveals the presence of several molecular clouds which have a good morphological agreement with the ionized gas. The CO structures are observed within the velocity range between -11 and 3 km s^{-1} compatible with the velocity of the H I structure and ionized gas as obtained by Cichowolski et al. (2001). Among the observed molecular clouds, four have been identified and characterized, over which several cYSOs are located.

At infrared wavelengths, the large-scale distribution of the *WISE* emission at 12 μm clearly shows the presence of a PDR bordering the H II region. In *Herschel* bands a shell-like structure is noticeable, showing a good morphological coincidence with the CO structures, suggesting that the dust coexists with the molecular gas. This is consistent with dust temperatures of about 24 K obtained for the shell structure.

On smaller scales, we see clear evidence of gas and dust being in the process of forming new stars, together with an accompanying erosion of the associated cloud, as a result of the combined action of the stellar UV radiation and wind of WR 130. This appears most clearly on the high-resolution *WISE* images which show morphological features (e.g. oriented pillars or thin filaments) generally seen around young massive stars or stellar clusters and which are indicative of stellar formation.

The presence of compact sources at the tip of some of these structures identifies these as probable YSOs. Two groups of such objects have been identified. In the first case, two of the compact IR sources have an associated weak radio source located on the star-facing side of their associated CO cloud. Using the available information, we have shown that these two cases are consistent, one formally and the second one marginally, with a formation via the RDI mechanism. The other sources, which have a more elongated or pillar-like appearance, do not have associated radio continuum counterparts and a similar analysis cannot be carried out. A different mechanism involving the curvature of a dense expanding shell leading to the formation of stable pillar-like structures has been proposed (Tremblin et al. 2012a,b, 2013) and could very well be a promising avenue to explain the observed features. However, such an analysis is clearly out of the scope of this paper.

Based on different colour criteria, an analysis of the YSO candidates in the vicinity of WR 130 has allowed us to estimate some of their physical parameters and revealed that most are in a very early phase of their formation, still accreting mass, and that they are mainly low-mass stars. An estimate of their age shows that, whereas the age gradient is as expected in some cases, there are nevertheless cases where the situation is uncertain. It is not clear whether this effect is real or the result of a poor fitting of the SEDs.

In summary, the morphological correlation between ionized and neutral gas as well as the ring-like dust emission confirm the high degree of interaction between the wind and UV photons from the WR star and the surrounding molecular clouds. In addition, the presence of numerous cYSOs within the molecular gas suggests that an active star formation process is taking place in the environs of this star.

ACKNOWLEDGEMENTS

We thank Tony Marston, the referee, for his careful reading of the manuscript and constructive comments that helped us to improve its substance & presentation. We thank Sergio Molinari and the HiGAL Consortium for making available to us the WR130 *Herschel* data. It is also a pleasure to thank Davide Elia and Eugenio Schisano (HiGAL Consortium members), for their help on the source extraction around the WR130 region, using the *Herschel* data. The CGPS is a Canadian Project with international partners and is supported by grants from NSERC. Data from the CGPS are publicly available through the facilities of the Canadian Astronomy Data Centre (http://cadc.hia.nrc.ca) operated by the Herzberg Institute of Astrophysics, NRC. We acknowledge Dr Christ Brunt who kindly made available the FCRAO CO data to us. This project was partially financed by the Consejo Nacional de Investigaciones CientÃficas y TÃ©cnicas (CONICET) of Argentina under project PIP 01299, Agencia PICT 00902, and UNLP G091. LAS is a postdoctoral

Downloaded from https://academic.oup.com/mnras/article-abstract/450/4/3458/992360 by guest on 04 September 2019

fellow of CONICET, Argentina, SC and EMA are members of the Carrera del Investigador CientÃfico of CONICET, Argentina.

REFERENCES

Anderson L. D. et al., 2012, A&A, 542, A10
Beichman C. A., Neugebauer G., Habing H. J., Clegg P. E., Chester T. J. eds., 1988, Infrared astronomical satellite (IRAS) catalogs and atlases. Volume 1: Explanatory supplement, Vol. 1
Benjamin R. A. et al., 2003, PASP, 115, 953
Bertoldi F., 1989, ApJ, 346, 735
Bohlin R. C., Savage B. D., Drake J. F., 1978, ApJ, 224, 132
Boulanger F., Abergel A., Bernard J.-P., Burton W. B., Desert F.-X., Hartmann D., Lagache G., Puget J.-L., 1996, A&A, 312, 256
Bronfman L., Nyman L.-A., May J., 1996, A&AS, 115, 81
Cappa C. E., Vasquez J., Pineault S., Cichowolski S., 2010, MNRAS, 403, 387
Carey S. J. et al., 2009, PASP, 121, 76
Castor J., McCray R., Weaver R., 1975, ApJ, 200, L107
Chaisson E. J., 1976, in Avrett E. H., ed., Frontiers of Astrophysics. Harvard Univ. Press, p. 259
Cichowolski S., Pineault S., Arnal E. M., Testori J. C., Goss W. M., Cappa C. E., 2001, AJ, 122, 1938
Compiègne M. et al., 2011, A&A, 525, A103
Conti P. S., Leep M. E., Perry D. N., 1983, ApJ, 268, 228
Crowther P. A., 2007, ARA&A, 45, 177
de Jager C., Nieuwenhuijzen H., van der Hucht K. A., 1988, A&AS, 72, 259
Deharveng L. et al., 2010, A&A, 523, A6
Dyson J. E., Williams D. A., 1997, in Dyson J. E., Williams D. A., eds, The Physics of the Interstellar Medium, 2nd edn. Adam Hilger, Bristol
Egan M. P., Price S. D., Kraemer K. E., 2003, in Bulletin of the American Astronomical Society, Vol. 35, American Astronomical Society Meeting Abstracts, p. 1301
Elia D. et al., 2013, ApJ, 772, 45
Elmegreen B. G., 1998, in Woodward C. E., Shull J. M., Thronson H. A., Jr, eds, ASP Conf. Ser. Vol. 148, Origins. Astron. Soc. Pac., San Francisco, p. 150
Evans N. J., II et al., 2009, ApJS, 181, 321
Fowler J. W., Aumann H. H., 1994, in Terebey S., Mazzarella J. M., eds, Science with High Spatial Resolution Far-Infrared Data. p. 1
Garcia-Segura G., Mac Low M.-M., 1995, ApJ, 455, 145
Griffin M. J. et al., 2010, A&A, 518, L3
Heckathorn J. N., Bruhweiler F. C., Gull T. R., 1982, ApJ, 252, 230
Heyer M. H., Brunt C., Snell R. L., Howe J. E., Schloerb F. P., Carpenter J. M., 1998, ApJS, 115, 241
Higuchi A. E., Kurono Y., Naoi T., Saito M., Mauersberger R., Kawabe R., 2013, ApJ, 765, 101
Jaschek M., Egret D., 1982, in Jaschek M., Groth H.-G., eds, Proc. IAU Symp. 98, Be Stars. Reidel, Dordrecht, p. 261
Junkes N., Fuerst E., Reich W., 1992, A&A, 261, 289
Kerton C. R., Martin P. G., 2000, ApJS, 126, 85
Koenig X. P., Leisawitz D. T., Benford D. J., Rebull L. M., Padgett D. L., Assef R. J., 2012, ApJ, 744, 130
Kohoutek L., Wehmeyer R., 1997, Astronomische Abhandlungen der Hamburger Sternwarte. Hamburger Sternwarte, Hamburg-Bergedorf, p. 11
Koo B.-C., McKee C. F., 1992, ApJ, 388, 103
Lefloch B., Lazareff B., 1994, A&A, 289, 559
Liu T., Wu Y., Zhang H., Qin S.-L., 2012, ApJ, 751, 68
Liu T., Wu Y., Zhang H., 2013, in Wong T., Ott J., eds, Proc. IAU Symp. 292, Molecular Gas, Dust, and Star Formation. Cambridge Univ. Press, Cambridge, p. 48
Lumsden S. L., Hoare M. G., Oudmaijer R. D., Richards D., 2002, MNRAS, 336, 621
Maíz Apellániz J. et al., 2013, Massive Stars: From α to Ω. p. 198
Mathis J. S., Mezger P. G., Panagia N., 1983, A&A, 128, 212
Mezger P. G., Henderson A. P., 1967, ApJ, 147, 471
Molinari S., Pezzuto S., Cesaroni R., Brand J., Faustini F., Testi L., 2008, A&A, 481, 345
Molinari S. et al., 2010, PASP, 122, 314
Molinari S., Schisano E., Faustini F., Pestalozzi M., di Giorgio A. M., Liu S., 2011, A&A, 530, A133
Morgan L. K., Urquhart J. S., Thompson M. A., 2009, MNRAS, 400, 1726
Nakanishi H., Sofue Y., 2006, PASJ, 58, 847
Paladini R. et al., 2012, ApJ, 760, 149
Piazzo L., Calzoletti L., Faustini F., Pestalozzi M., Pezzuto S., Elia D., di Giorgio A., Molinari S., 2015, MNRAS, 447, 1471
Pilbratt G. L. et al., 2010, A&A, 518, L1
Pineault S., 1998, AJ, 115, 2483
Poglitsch A. et al., 2010, A&A, 518, L2
Reed B. C., 2003, AJ, 125, 2531
Robitaille T. P., Whitney B. A., 2014, in Stamatellos D., Goodwin S., Ward-Thompson D., eds, Astrophysics and Space Science Proc. Vol. 36, The Labyrinth of Star Formation. Springer-Verlag, Berlin, p. 157
Robitaille T. P., Whitney B. A., Indebetouw R., Wood K., Denzmore P., 2006, ApJS, 167, 256
Robitaille T. P., Whitney B. A., Indebetouw R., Wood K., 2007, ApJS, 169, 328
Rodón J. A. et al., 2010, A&A, 518, L80
Schwartz P. R., 1985, ApJ, 298, 292
Smith N., Conti P. S., 2008, ApJ, 679, 1467
Stock J., Nassau J. J., Stephenson C. B., 1960, Hamburger Sternw. Warner Swasey Obs., 2, 0
Tan J. C., Beltrán M. T., Caselli P., Fontani F., Fuente A., Krumholz M. R., McKee C. F., Stolte A., 2014, in Beuther H., Klessen R. S., Dullemond C. P., Henning T., eds, Protostars and Planets VI. Univ. Arizona Press, Tuscan, AZ, p. 149
Taylor A. R. et al., 2003, AJ, 125, 3145
Traficante A. et al., 2011, MNRAS, 416, 2932
Tremblin P., Audit E., Minier V., Schmidt W., Schneider N., 2012a, A&A, 546, A33
Tremblin P., Audit E., Minier V., Schneider N., 2012b, A&A, 538, A31
Tremblin P. et al., 2013, A&A, 560, A19
Urquhart J. S., Hoare M. G., Lumsden S. L., Oudmaijer R. D., Moore T. J. T., 2008, in Beuther H., Linz H., Henning T., eds, ASP Conf. Ser. Vol. 387, Massive Star Formation: Observations Confront Theory. Astron. Soc. Pac., San Francisco, p. 381
Urquhart J. S. et al., 2009, A&A, 501, 539
Urquhart J. S. et al., 2011, MNRAS, 418, 1689
van der Hucht K. A., 2001, New Astron. Rev., 45, 135
Wackerling L. R., 1970, MNRAS, 73, 153
Weaver R., McCray R., Castor J., Shapiro P., Moore R., 1977, ApJ, 218, 377
Wright E. L. et al., 2010, AJ, 140, 1868
Zavagno A. et al., 2010, A&A, 518, L81

This paper has been typeset from a TEX/LATEX file prepared by the author.

Downloaded from https://academic.oup.com/mnras/article-abstract/450/4/3458/992360 by guest on 04 September 2019